Three-dimensional study of Mars upper thermosphere/ionosphere and hot oxygen corona: 2. Solar cycle, seasonal variations, and evolution over history

Arnaud Valeille,[1] Michael R. Combi,[1] Stephen W. Bougher,[1] Valeriy Tenishev,[1] and Andrew F. Nagy[1]

Received 26 March 2009; revised 5 June 2009; accepted 8 July 2009; published 7 November 2009.

[1] The global dynamics of the flow of energetic particles through the Martian upper atmosphere is studied for different cases reflecting variations in solar cycle, seasons, and epochs over history. In this study, the combination of the new 3-D Direct Simulation Monte Carlo kinetic model and the modern 3-D Mars Thermosphere General Circulation Model is employed to describe self-consistently the Martian upper atmosphere (i.e., the thermosphere/ionosphere and the exosphere). The variations in the Martian upper atmosphere over long-term (seasons and solar cycle) and evolutionary (Martian history) time scales are presented and discussed using the equinox solar low case extensively described in the work of Valeille et al. (2009c) as reference throughout. These characteristic conditions lead to significant variations in the thermosphere/ionosphere temperatures, dynamical heating, winds, and ion/neutral density distributions, which, in turn, affect the exosphere general structure, the hot corona shape, and the escape rate and have important implications for the study of the ion loss, atmospheric sputtering, and interaction with the solar wind in general. Calculations for present conditions are performed for three characteristic seasons (aphelion, equinox, and perihelion), while solar activity is either fixed to low or high conditions. Calculations for past conditions are related to a solar EUV flux enhancement of 1, 3, and 6 times the present values. Spatial-, seasonal-, solar cycle–, and evolutionary-driven variations, although exhibiting very different time scales, are all shown to exert an influence of the same order. Models of Mars upper atmosphere should address them accordingly.

Citation: Valeille, A., M. R. Combi, S. W. Bougher, V. Tenishev, and A. F. Nagy (2009), Three-dimensional study of Mars upper thermosphere/ionosphere and hot oxygen corona: 2. Solar cycle, seasonal variations, and evolution over history, *J. Geophys. Res.*, *114*, E11006, doi:10.1029/2009JE003389.

1. Introduction

[2] Processes that shape the exosphere and the Martian hot corona originate deep in the thermosphere/ionosphere. Therefore, independently of the complexity of the exosphere model used for calculations, the limitations are inherent to the thermosphere/ionospheric inputs employed. It is therefore highly desirable to employ a global kinetic model that includes a self-consistent description of both regions to provide a rigorous description of the exosphere, the hot corona and the atmospheric loss.

[3] Keeping this in mind, the study of *Valeille et al.* [2009a] couples for the first time 3-D thermospheric/ionospheric inputs [e.g., *Bougher et al.*, 2006, 2008, 2009] with a 2-D exospheric description. It suggests, in particular, that varying equatorial longitude and polar latitude cuts, i.e., calculations from 0° to 180° Solar Zenith Angle (SZA) along the equator or through the poles, present the greatest contrasts of thermospheric/ionospheric features and are essentially the two extreme spatial dimensions of the Martian upper atmosphere environment (i.e., thermosphere/ionosphere and exosphere).

[4] The same study quantifies not only the influence of the solar cycle, but also of seasons on the thermosphere/ionosphere and exosphere by characterizing the two extreme cases of net solar forcing for present conditions, i.e., aphelion solar low (AL) and perihelion high (PH). Conclusions show that seasonal variations are comparable with the influence of solar activity, and that they both need to be addressed for a better understanding of the Martian upper atmosphere.

[5] The same approach is used to study the evolution of the thermosphere/ionosphere and exosphere over Martian history in the study of *Valeille et al.* [2009b]. The inclusion of dynamics shows that it plays a very important role in the heating/cooling mechanisms of the ancient thermosphere and that past 1-D models, which inherently neglect dynamics [*Zhang et al.*, 1993b; *Lammer et al.*, 2003], may have

[1]Department of Atmospheric, Oceanic and Space Sciences, University of Michigan, Ann Arbor, Michigan, USA.

Copyright 2009 by the American Geophysical Union.
0148-0227/09/2009JE003389

overestimated the exospheric temperatures and therefore the structure of the upper atmosphere in general. The study of *Valeille et al.* [2009b] further concludes that variations due to ancient solar conditions and modern solar activity are comparable and therefore that studies of the ancient atmosphere should take into account solar low and high conditions to bracket the limiting cases (or at least consider solar moderate as a solar cycle average in the past), as suggested in the recent study of *Chassefière et al.* [2007].

[6] The work of *Valeille et al.* [2009c] couples a 3-D thermosphere/ionosphere model with a 3-D exosphere code and studies spatial variations with altitude and with angular position on the planet (diurnal and local features) in the upper atmosphere. The simulation is run at fixed conditions of equinox solar low (EL), for comparison sake with the only in situ measurements available today of the Viking 1 and 2 mission descents [e.g., *Hanson et al.*, 1977; *Nier and McElroy*, 1977]. It concludes that the thermospheric/ionospheric parameters exhibit local asymmetries that affect the entire structure of the upper atmosphere.

[7] A complete description by a steady state simulation requires two types of parameters to be investigated: spatial and temporal. So, while the previous study of *Valeille et al.* [2009c] describes the spatial distribution of the upper atmosphere in the fixed EL case, this paper focuses on the variation of the thermosphere/ionosphere and exosphere parameters over all the principal time scales. Temporal perturbations can be distinguished by their characteristic time: short scale ($\sim$1 h), long scale ($\sim$1–10 year) and evolutionary scale ($\sim$1 Gyr). A recent study [*Kaneda et al.*, 2007, 2009] indicates a possible mechanism that can cause a short-term (about 2000 s period) enhancement of the hot oxygen escape rate in response to a sudden increase in the solar wind dynamic pressure.

[8] In this paper, the variations in the Martian upper atmosphere over long-term (seasons and solar cycle) and evolutionary (Martian history) time scales are presented and discussed using the EL case extensively described in the work of *Valeille et al.* [2009c] as a reference throughout. These variations affect the thermosphere/ionosphere temperatures, winds and ion/neutral density distributions, the exosphere general structure, the hot corona shape, and the ion/neutral loss, and have important implications for the study of the interaction with solar wind.

2. Model and Assumptions

[9] The two 3-D models used in combination in this work, the 3-D Mars Thermosphere General Circulation Model (MTGCM) and the 3-D Direct Simulation Monte Carlo (DSMC), were extensively described along with how they are coupled in a previous paper [*Valeille et al.*, 2009c]. The main detailed assumptions used in the description of the Martian upper atmosphere regarding solar cycle and seasons are listed in the work of *Valeille et al.* [2009a], while the assumptions regarding the Martian history are presented in detail in the work of *Valeille et al.* [2009b]. Only brief descriptions are given again in this section.

2.1. Model Description: MTGCM

[10] The modern MTGCM is a finite difference primitive equation model that self-consistently solves for time-dependent neutral temperatures, neutral ion densities, and three component neutral winds over the globe [*Bougher et al.*, 2004, 2006, 2008, 2009]. A fast non-Local Thermodynamic Equilibrium (NLTE) 15-μm cooling scheme is implemented, along with corresponding near Infra Red (IR) heating rates [*López-Valverde et al.*, 1998; *Bougher et al.*, 2006]. The MTGCM is driven from below by the NASA Ames Mars General Circulation Model (MGCM) code [*Haberle et al.*, 1999] at the 1.32 μbar level (near 60–80 km). The MGCM-MTGCM framework incorporates a detailed photochemical ionosphere, which captures the major ions, O_2^+, CO_2^+, O^+, and NO^+, below 180 km [*Bougher et al.*, 2004]. Additional MTGCM details can be found in the work of *Bougher et al.* [2004, 2006, 2008].

2.2. Model Description: DSMC

[11] The DSMC model is a 3-D simulator that solves for the coupled thermosphere/ionosphere and exosphere systems using an altitude-based coordinate system [see *Valeille et al.*, 2009c]. Instead of assuming a strict separation between collision and collisionless domains, the DSMC model considers a collision transitional domain where the momentum exchange within the flow is still important but the collision frequency is not high enough to maintain equilibrium in the flow. A probabilistic technique is used to sample the state of collision partners after a momentum exchange event, to simulate scattering and chemical reactions. The approach [*Tenishev et al.*, 2008] is based on solving the Boltzmann equation and, hence, is valid for all gas flow regimes presented in the domain of study. It provides a complete set of the exospheric macroscopic parameters for hot oxygen, its escape flux, and its return flux to the thermosphere.

[12] The code uses an unstructured mesh of tetrahedral cells that allows a pertinent description of the domain around complex 3-D bodies. It can be easily adapted to the physical features of the problem, and takes into account the variations of the outputs of interest. The angular resolution matches that of the thermosphere model, being a $5^\circ \times 5^\circ$ grid all across the simulation domain. The mesh presents uniformly spaced cells distributed radially from the inner boundary (at 135 km) to 200 km with a 4 km altitude resolution, followed by exponentially distributed cells beyond the 200 km altitude. This allows for an approximately constant number of atmospheric particles per cell (mostly $\sim$20–40 particles per cell). The size of the simulation domain is limited to a 3-Mars-radius domain of interest for most studies in order to limit the computational time and to keep the two-body approximation valid. A total of about 500,000 cells, or 30 million particles, is simulated.

[13] The 3-D Cartesian frame used in this work is slightly different from the one in the work of *Valeille et al.* [2009c], as the tilt due to the seasons has now to be taking into account. It is associated with the Sun, has its origin at the center of the planet, the x axis pointing toward the equator at noon (in case of Equinox, this would be toward the Sun), the y axis toward the east terminator and the z axis toward the north pole. It is important to note that, since steady state is assumed (i.e., the results will not be affected by the longitudinal variations during the course of a planet day), in

Table 1. Impact of Season and Solar Cycle on Thermospheric/Ionospheric Parameters

	Orbital Position		
Solar Activity	Aphelion	Equinox	Perihelion
	Neutral Temperature[a]		
Low	90/165/260	115/175/290	100/185/260
High		155/260/370	155/310/360
	Global Average O Density at 165 km[b]		
Low	4.8	6.5	8.4
High	8.9	13.0	15.0
	Electron Density at Subsolar Point[c]		
Low	1.8	2.0	2.1
High	2.7	3.1	3.2
	Ion Peak Height at Subsolar Point[d]		
Low	116	122	128
High	116	122	128
	Average Exobase Height[d]		
Low	165	170	180
High		185	195

[a]Minimum/average/maximum, in K.
[b]Values in $\times 10^7$ cm^{-3}.
[c]Values in $\times 10^5$ cm^{-3}.
[d]Values in km.

this framework, the 0° longitude is fixed at local noon (UT = 12).

3. Season and Solar Cycle Variations

[14] While variations of the hot corona with solar activity have been previously studied by two- and three-dimensional models that use extrapolation of 1-D thermospheric/ionospheric inputs [*Hodges*, 2000; *Kim et al.*, 2001; *Chaufray et al.*, 2007], this global 3-D study considers both solar cycle conditions, low and high, and seasonal variations, named for the remainder of this paper after the corresponding orbital position of aphelion, equinox, and perihelion (which constitute for the northern hemisphere: summer, spring/autumn, and winter, respectively).

[15] Solar cycle influences are characterized at a fixed orbital position of equinox by comparing equinox solar low case with equinox solar high (EH) case. Seasonal influences are characterized at a fixed solar activity of solar low by comparing aphelion solar low case, with EL case and with perihelion solar low (PL) case. These notations are used in the remainder of the paper. The combined effects of these long-term variations can be characterized by the two extreme net solar forcing cases at present of aphelion solar low and perihelion solar high. A similar approach is used in the study of *Valeille et al.* [2009a] along the equator and the polar meridian.

3.1. Thermosphere/Ionosphere

3.1.1. Temperatures, Heating, and Winds

[16] In the cold isothermal region of the Martian atmosphere, i.e., in the upper thermosphere until approximately 600 km altitude [*Valeille et al.*, 2009a], the average neutral exospheric temperature, T_∞, is about 170–180 K for the EL case. It is mostly located at low and middle latitudes on the dayside and high latitudes on the nightside. High temperatures are found on the dayside along the terminator, maxima of about 250–290 K being at the dayside polar regions and in the vicinity of the evening terminator. Minimum temperatures of about 115–130 K are situated south, at low and middle latitudes on the nightside [*Valeille et al.*, 2009c].

[17] The spatial distribution of temperature averages and extrema, and the temperature structure in general, stays the same from the EL to the EH case. However, the increase in the EUV flux leads to higher dayside average and maximum temperatures of about +100–110 K. The dynamics, which effectively cools the dayside and heats the nightside, tends to homogenize the temperatures, and the nightside is then affected to a lesser extent (about +50 K) by the solar cycle variation (see Table 1).

[18] Due to Mars important eccentricity, the change in the heliocentric distance with orbital position of the planet leads to a significant variation in the EUV flux at the top of the atmosphere [e.g., *Bougher et al.*, 1999, 2000]. While the average temperature changes slightly from 160 to 170 K for the AL case to 180–190 K for the PL case, the axial tilt (of a maximum of ±25.19° during solstices) changes the spatial distribution dramatically. Polar regions are either at constant night or day, affecting the entire global temperature structure and the global dynamics. Minima are more pronounced (about −20 K) for solstices than for the equinox cases and are located on the nightside equator between the antisolar point (i.e., 180° SZA) and the opposite hemisphere mid latitudes (dark blue areas in Figure 1b, light blue areas in Figure 1d). Maxima are on the dayside equator between the subsolar point (i.e., 0° SZA) and the opposite hemisphere mid latitudes, as well as in the morning in the summer hemisphere (green areas in Figure 1b, orange areas in Figure 1d). They are also slightly lower than for the EL case (by about −20 K) since the dynamical cooling due to vertical winds is more efficient in these regions. Linear regression of average dayside temperatures, a function of the F10.7cm index scaled to Mars (between F10.7cm = 20 and 110, corresponding to the AL and PH cases, respectively) leads to a slope dT/dF10.7cm of about 1.45–1.68, in good agreement with the reported observation of about 1.5 [*Forbes et al.*, 2008].

[19] In the frame associated with Mars, the general circulation pattern in the vicinity of the exobase is essentially toward the west (opposed to the planetary rotation direction and with a comparable magnitude) with a minimum at the evening terminator and maximum (of about 490 m s^{-1}) at the morning terminator. Coriolis effects are noticeable at high latitudes (see Figures 1b and 1d). The trend stays the same with solar activity, with slightly stronger average winds for the EH case. In the solstice cases, the winds present more complex features than the equinox cases and are mostly oriented toward the winter pole (see Figures 1b and 1d). The PL case exhibits stronger winds (maximum at 435 m s^{-1}) than the AL case (maximum at 390 m s^{-1}), as both solar heating and dust opacity are higher, further strengthening the wind system [*Bougher et al.*, 2006].

[20] According to *Bougher et al.* [1999, 2000, 2009], the primary dayside balance in the modern Martian thermosphere occurs between EUV heating and molecular thermal conduction, with CO_2 cooling playing a tertiary role. In addition, Mars adiabatic cooling, due to rising motions on the dayside from the global circulation, should play a progressively more important role as the solar cycle advances. This "dynamical thermostat" cannot be ignored when

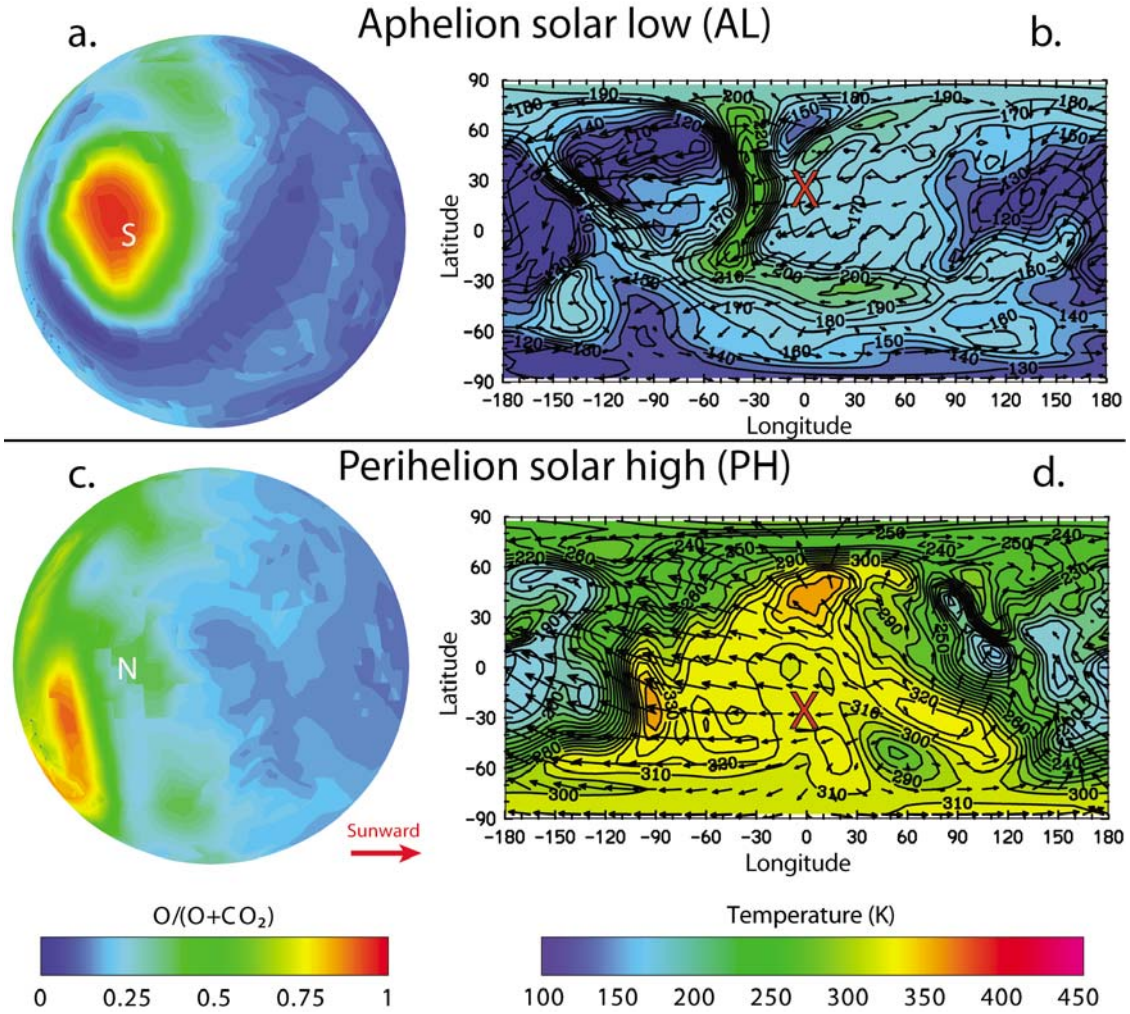

Figure 1. Oxygen mixing ratio in the winter hemisphere and neutral temperature in the vicinity of Mars exobase for the two most extreme cases for present conditions. The results are shown at the respective average exobase level, i.e., at an altitude of (a and b) 165 km for the AL case and (c and d) 195 km for the PH case. Horizontal wind velocities are represented in the frame associated with Mars by arrows with maxima at ~390 (Figure 1b) and ~555 m s^{-1} (Figure 1d). The same color scale is used for each image and is consistent with that for Figure 5. The red crosses mark the subsolar point. The north and south pole positions are indicated by N and S, respectively. The red arrow points toward the Sun.

examining the heat balances, giving rise to solar cycle and seasonal variations of Martian thermospheric neutral temperature. 3-D models are thus essential for a proper investigation of Martian thermospheric heat balances [*Bougher et al.*, 2000, 2009]. Furthermore, it is important to account for these effects as they relate to and produce a proper 3-D corona.

3.1.2. O and CO_2 Density Distribution

[21] Mars upper atmosphere presents two major neutral constituents, carbon dioxide and atomic oxygen. For the EL case, atomic oxygen reaches its maximum densities at low latitudes on the nightside near the morning terminator where the winds are stronger and converge, whereas minima are reached on the dayside close to the evening terminator where winds are weaker and diverge [*Valeille et al.*, 2009c]. Carbon dioxide reaches its maximum densities in the polar regions where temperatures are warmer. Similarly, minima are achieved at low latitudes on the nightside near the morning terminator where temperatures are colder.

[22] For the EH case, density profiles extracted along 1-D columns exhibit a scale height temperature that matches the average neutral temperature of $T_\infty \sim 260$ K. The spatial distribution is very similar to that in the upper atmosphere in the EL case. At a given altitude, an enhancement in density of a factor of about $\times 1.8-2.0$ is computed due to solar activity (Table 1). This increase in the background densities at a fixed altitude is due to higher thermospheric temperatures for solar high, that affect the scale heights of the constituents proportionally, resulting in a global expansion of the atmosphere.

[23] It is logical to expect large variations with seasons in the spatial distributions of the background species. Indeed, O and CO_2 densities are driven locally by the respective effect of dynamics and temperature [*Valeille et al.*, 2009c], which are shown to vary significantly (see Figures 1b and 1d). Atomic oxygen reaches its maximum densities at the winter pole (i.e., south pole for aphelion, and north pole for perihelion), whereas carbon dioxide does so at the

summer pole (vice versa). Both species reach minima between the summer pole and the antisolar point. An enhancement in density of a factor of about $\times 1.7-1.8$ is estimated, and the differences between extrema are more pronounced for the solstice cases (about $\times 30$ for O) compared to the equinox cases (about $\times 10$ for O).

[24] As shown in the work of *Valeille et al.* [2009c], the O mixing ratio, $O/(O + CO_2)$, not only varies greatly with the altitude (due to different scale heights above the homopause and the CO_2 molecule being heavier than O atom), but also with the angular position on the planet (due to local features of thermospheric temperature and dynamics). Indeed, CO_2 is more responsive to the background temperature, while O is more responsive to the winds. Figures 1a and 1c show maps of the oxygen mixing ratio for the two most extreme cases combining the effects of solar activity and seasons for present conditions. It presents a clear illustration of additional implications of the winter polar warming effect [*Bougher et al.*, 2006], exhibiting a peak in the atomic oxygen concentration in the winter polar region. These should be considered in context with Figures 1b and 1d, which present strong convergent winds and a vortex circulating toward the winter polar regions, where the only heating mechanism is dynamics (as opposed to the EUV heating on the dayside). This is in good agreement with the measurements by the ultraviolet spectrometer (SPICAM) instrument onboard Mars express (MEX) of the nitric oxide night airglow [*Bertaux et al.*, 2005]. Indeed, atomic oxygen and nitrogen, tracers of the circulation, were observed blowing from the dayside toward the winter pole.

3.1.3. O_2^+ Distribution and Ionospheric Peak

[25] O_2^+ is the main ion of the Martian ionosphere and its distribution is closely related to both local solar radiation and density of the bulk atmosphere (O and CO_2 being its parents via photodissociation and charge exchange reactions). As a result, it is located mostly on the dayside, and its abundance undergoes significant variations spatially and with solar cycle and seasons.

[26] For present conditions, O_2^+ DR is by far the most important source of hot oxygen in the Martian thermosphere. The cumulative effect of the escape processes resulting from the interaction of the solar wind onto the Martian corona (including sputtering and ion escape) appears to be smaller by at least 1 order of magnitude than the contribution due to O_2^+ DR at the present epoch according to recent studies [*Leblanc and Johnson*, 2001; *Chaufray et al.*, 2007]. The excess energies and the measured branching ratios of *Kella et al.* [1997] are used for the main branches of the O_2^+ DR reaction. In this work, the O_2^+ DR reaction rate coefficient is taken from *Mehr and Biondi* [1969].

[27] For the EL case, the ionospheric peak is found to be deep in the thermosphere at an altitude of about $\sim$122 km at the subsolar point [*Valeille et al.*, 2009c]. Its magnitude, defined as the local electron density there, is estimated to be 2.0×10^5 cm^{-3}. Both height and magnitude are affected by solar radiation. The peak height is controlled by the underlying lower atmosphere, which is not greatly impacted by changing EUV-UV fluxes, but rather IR fluxes, while the peak magnitude and the region above it are more responsive to EUV radiation.

[28] Solar activity is mostly characterized by variations in EUV radiation. So, while the altitude of the peak does not rise appreciably with the solar cycle, the magnitude of the ion peak, the electron density increases to 3.1×10^5 cm^{-3} at the subsolar point for the EH case (Table 1).

[29] Seasonal influence is mostly characterized by variations in the long waves and IR fluxes, decreasing with increasing heliocentric distance. This radiation is absorbed in the lower part of the atmosphere which expands as a result. Therefore the ion peak, homopause and exobase heights rise together by about $+12-15$ km from the AL case to the PL case (Table 1). At the subsolar point, the ion peak height is then found at 116 and 128 km altitude for the aphelion and perihelion cases, respectively. The homopause is determined to vary in the very similar range of altitudes (115–130 km) [*Stewart*, 1987; *Bougher et al.*, 2000].

[30] In all cases considered, the ion peak height increases, while its magnitude decreases with increasing SZA on the dayside [*Valeille et al.*, 2009c], in good agreement with the reported observations of Viking [*Zhang et al.*, 1990], Mars Global Surveyor (MGS) [*Withers and Mendillo*, 2005] and Mars Express (MEX) [*Morgan et al.*, 2008]. Finally, spatial distribution of O_2^+ follows the background species local abundances and, because of higher concentration of ions in the polar region compared to lower latitudes (especially in the case of solstices), the magnitude of the ion peak undergoes a milder decrease and the ion peak height a sharper increase with SZA along the meridian than along the equator.

3.1.4. Exobase Altitude

[31] Rigorously, the exobase level should be defined locally and for a transitional domain of multiple constituents. It is conservatively referred to the level above which an escaping particle moving along a radial direction will encounter one collision on average [*Valeille et al.*, 2009c]. For the EL case, the exobase height undergoes significant spatial variations, reaching its lowest value of 155 km along the dayside terminator and at nightside low and middle latitudes, whereas the highest value of 195 km can be found in the polar regions [*Valeille et al.*, 2009c]. It depends on the density of the bulk atmosphere, the mixing ratio of O/CO_2 and the temperature.

[32] The exobase height exhibits a similar rise of about +15 km with solar activity and season, but for different reasons (Table 1). The average exobase level rises from about 170 to 185 km altitude from the EL to the EH cases because of higher EUV heating, which occurs in the region above $\sim$140 km, resulting in warmer temperatures and the general expansion of the upper atmosphere. These variations are not as large as 1-D models predicted [e.g., *Ip*, 1990], since they could not capture the important dynamical effects. As mentioned above, the lower atmosphere (below 120 km) expands from the AL case to the PL case, resulting in a similar rise of the exobase height from 165 to 180 km altitude, respectively.

3.2. Exosphere

3.2.1. Density and Escape Flux Variations With Solar Activity

[33] Above the transitional region (i.e., above $\sim$600 km altitude), the oxygen population is "hot," i.e., dominated by the suprathermal population (the criteria used in this study is

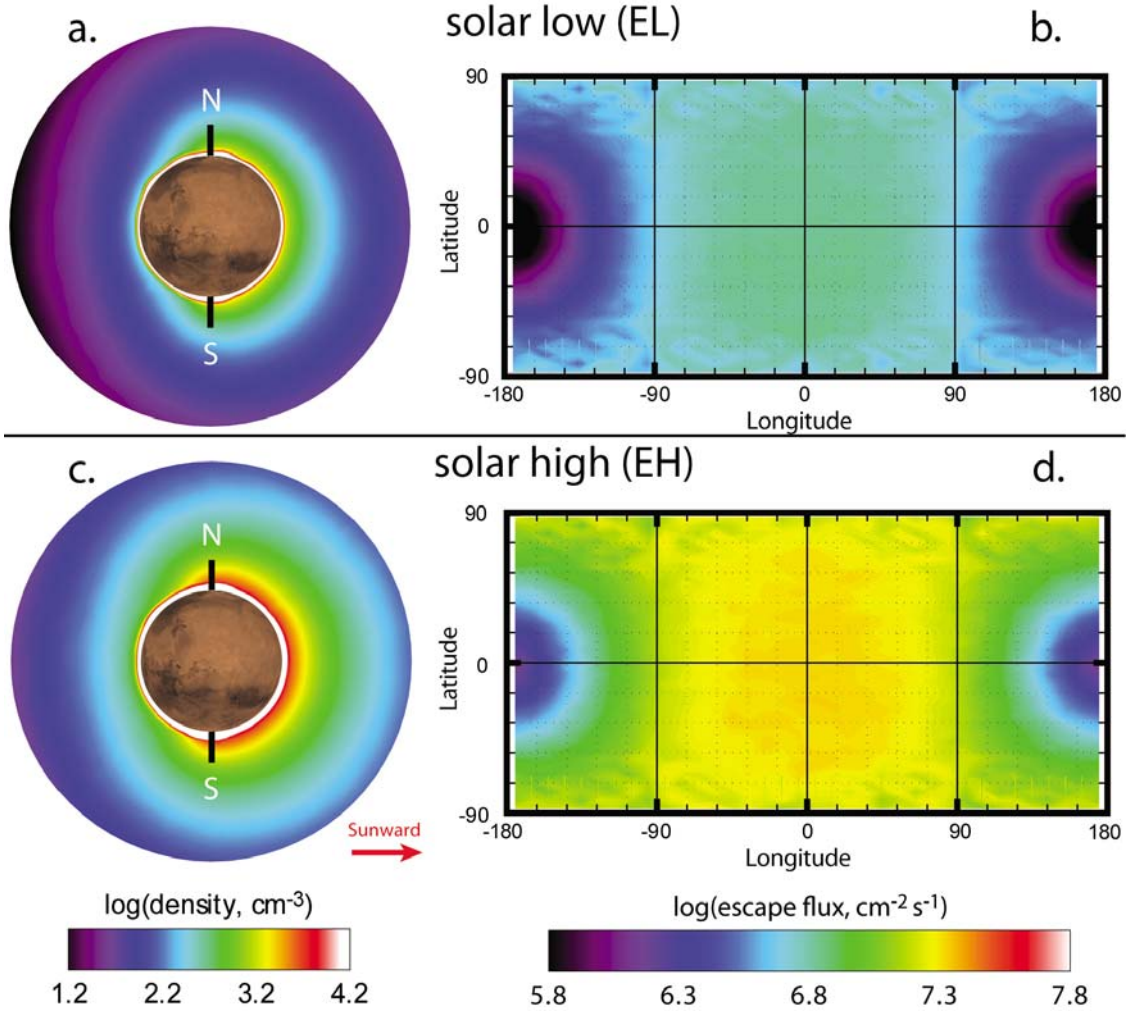

Figure 2. (a and c) Density profiles and (b and d) escape fluxes at 3 Martian radii of oxygen atoms at EL (Figures 2a and 2b) and EH (Figures 2c and 2d) conditions. The same color scale is used for each image and is consistent with that for Figures 3 and 6. The north and south pole positions are indicated by N and S, respectively. The red arrow points toward the Sun.

$V_{threshold}$, which is defined as twice the local thermal speed in the transitional domain) [*Valeille et al.*, 2009a] and the scale height temperature is about $T_{hot} \sim 4000$ K, independent of the EUV inputs. Spatial distributions of the density for the EL case (Figure 2a) and for EH case (Figure 2c) are very similar, with density maxima located south of the subsolar point and minima achieved in the vicinity of the antisolar point at an altitude of 7000 km (i.e., 3 radii from the center of the planet). The shape of the hot corona is clearly inflated toward the dayside. At a given altitude, a uniform global enhancement in densities of a factor about $\times 3$ is estimated over the solar cycle.

[34] The spatial distribution of the escape flux is also very similar between the two cases and illustrated at 3 radii in Figures 2b and 2d, for EL and EH cases, respectively. Rather than an axisymmetric circular shape with respect to the subsolar point, it exhibits an oblong shape centered south of it and extends toward the poles. The difference between extrema is a factor of about $\times 10$ at 3 radii, and decreases to about $\times 4$ at 10 radii [*Valeille et al.*, 2009a]. The total escape rate increases by a factor $\times 3$–4 from 6.0×10^{25} s^{-1} for the EL case to 1.9×10^{26} s^{-1} for the EH case (Table 2).

3.2.2. Density and Escape Flux Variations With Seasons

[35] While seasonal variations are impacting the spatial distribution of most of the thermosphere parameters, their global effect is milder further away from the exobase, since the exosphere tends to homogenize the density due to average value over wider area. In the frame associated with the Sun, the spatial distribution of the density profiles between different seasons presents only slight variations, as illustrated at solar low activity in Figures 3a, 3c, and 3e for the AL, EL, and PL cases, respectively. Also, at a given

Table 2. Impact of Season and Solar Cycle on the Escape Rate of Suprathermal Oxygen Atoms

	Orbital Position		
Solar Activity	Aphelion	Equinox	Perihelion
Low	4.6×10^{25}	6.0×10^{25}	7.4×10^{25}
High		1.9×10^{26}	2.6×10^{26}

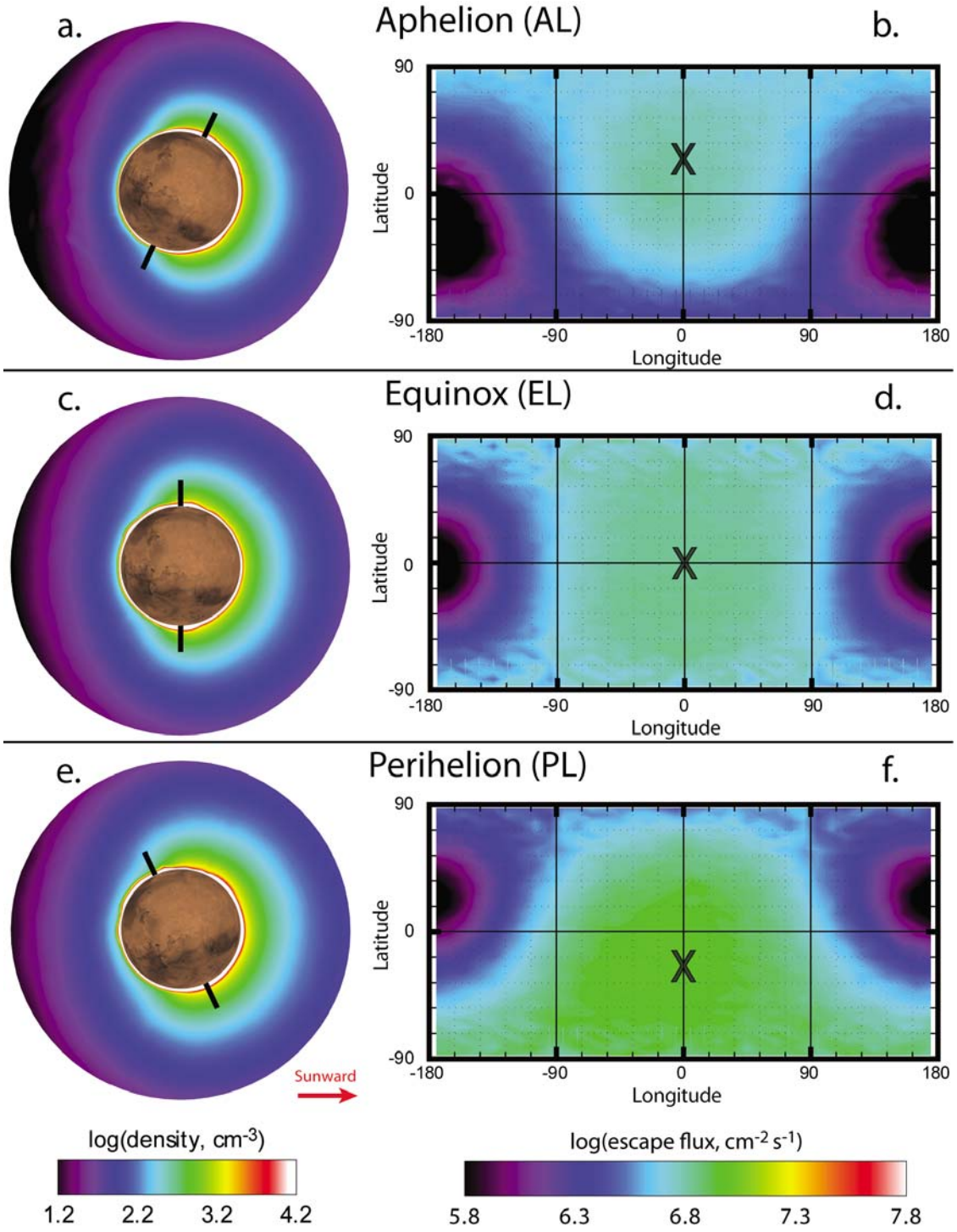

Figure 3. (a, c, and e) Density profiles and (b, d, and f) escape fluxes at 3 Martian radii of oxygen atoms for solar low activity at AL (Figures 3a and 3b), EL (Figures 3b and 3c) and PL (Figures 3e and 3f). The same color scale is used for each image and is consistent with that for Figures 2 and 6. The black crosses mark the subsolar point. The north and south pole positions are indicated by N and S, respectively. The red arrow points toward the Sun.

altitude, the local densities undergo a milder increase between AL and PL (seasonal effect) than between EL and EH (solar cycle effect).

[36] While, to first order, the equinox escape map is roughly axisymmetric with respect to the Mars-Sun axis (as shown for the EL case in Figure 3d), the axial tilt corresponding to the solstices cases has a very noticeable impact on the structure of the escape flux map (U shaped for the aphelion case, AL, in Figure 3b and reversed U shaped for the perihelion case, PL, in Figure 3f). The peak of

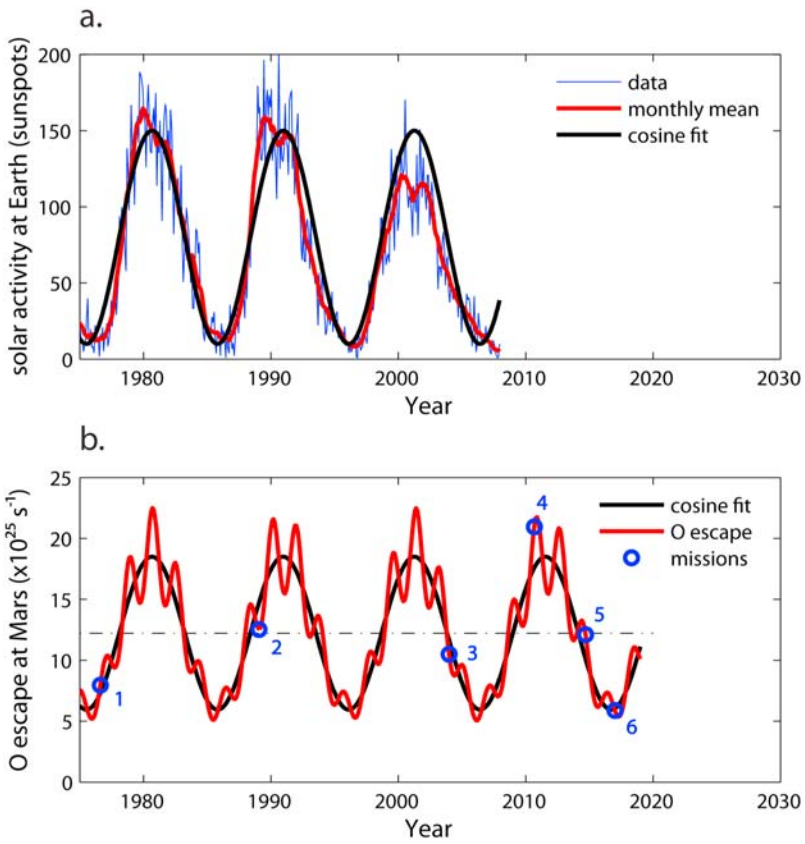

Figure 4. (a) Trends of the measured solar activity at Earth (1 AU). The daily sunspot number data, as reported by the Royal Observatory of Belgium, are represented in blue, the monthly averages are represented in red, and the cosine fit is represented in black. (b) Extrapolation and prediction of the total oxygen escape rate at Mars by the current study. The average computed escape rated is represented by the black dashed-dotted line. The cosine fit at the average orbit (∼1.5 AU) is represented in black, and the modulation due to orbital position is represented in red. Arrivals at Mars of past, current, and future missions to Mars (equipped with instruments capable of upper atmospheric density measurements) are numbered and represented by blue circles (see details in the text).

escape is still at the subsolar point but this location is shifted to +25° north latitude at aphelion and −25° south latitude at perihelion. The total escape rate increases from 4.6 for the AL case to 7.4×10^{25} s^{-1} for the PL case (Table 2). The relative variation with season in the escape rate is a factor about ×1.6, which is close to the theoretical ratio of $\sim(1.67/1.38)^2 \sim 1.46$ if the variation in the heliocentric distance only was considered between the two cases [*Valeille et al.*, 2009a]. However, seasonal variations, as defined in this study, include more than the orbital position, but also the effect of the obliquity, dust activity and hemispheric asymmetries that result in important changes in the lower atmosphere, and therefore affect both thermosphere and exosphere [*Bougher et al.*, 2006].

3.3. Discussion

[37] Table 2 illustrates the comparable impacts on the atmospheric loss of two long-term temporal variations: solar cycle (about an 11-year period) and the seasonal effect (about a 2-year period). In this section, a periodic trend of these phenomena is estimated and scaled to the results of the simulation in order to get a qualitative understanding of their cumulative variation with time.

[38] The International Sunspot Number, previously known as the Zürich series, is often used as an index of solar activity (in blue in Figure 4a). Data are taken from the homepage of the Solar Influences Data Analysis Center (SIDC; available at http://sidc.oma.be/). F10.7 has been shown to follow the sunspot number quite closely and similar prediction techniques can be used. They both are closely related to solar activity. Its short-term and long-term prediction is highly important for space weather applications [*Podladchikova et al.*, 2007]. A monthly average (in red in Figure 4a) is used in order to eliminate the difference of orbital position of Mars and Earth with respect to the Sun (the Sun rotation being ∼25.4 days). A cosine approximation fits reasonably well the variations and the last three cycles in particular, as shown in Figure 4. The solar minimum reference was taken on June 2006.

[39] Under the simple assumption that escape rate is proportional to solar radiation, the cosine fit is then used to approximate the variation of the escape rate with solar activity at Mars semimajor axis (i.e., about 1.52 AU from the Sun) in black in Figure 4b and extended for predictions of the near future. While Earth orbit is nearly circular, Mars orbit is highly elliptical. The modulation due to the seasonal

effect is approximated by an ellipse (in red in Figure 4b). The heliocentric distance at aphelion is 1.67 AU, while perihelion is 1.38 AU. The period is 687 days and the perihelion reference is taken on August 2003.

[40] This illustrates clearly that solar cycle and seasons have a comparable and significant influence on the escape and therefore both effects should be taken into consideration for a rigorous description. Indeed, the cumulative effect of these long-term periodic variations is estimated to be a factor of about $\times 6$ in the atmospheric loss between the two extreme cases of AL and PH, setting a lower and upper limit for the modern conditions. Those results have important implication for ion production, and therefore the population of the ionosphere that in turn regulates ion escape and sputtering in its interaction with the solar wind.

[41] Past and future missions to Mars relevant to the oxygen escape are represented as blue circles in Figure 4b. The only in situ measurements of the Martian upper atmosphere currently available are from Viking 1 and 2 mission descents corresponding to the EL case (1 in Figure 4b). Since then, the ASPERA 1 and 3 instruments onboard Phobos 2 and MEX (2 and 3 in Figure 4b, respectively) provided valuable indirect information from ionospheric observations for solar moderate to high and mostly solar low conditions, respectively. While the instruments on the Viking missions could not detect the hot oxygen corona, the upcoming missions, Phobos-Grunt and Yinghuo-1, Mars Scout Mission and ExoMars scheduled to arrive in 2011, 2014, and 2017 (4, 5, and 6 in Figure 4b, respectively) may be able to measure densities of hot oxygen around Mars for an extended period of time. Indeed, depending of the interval of sampling (looking at Figure 4b), measurements over a year might be enough to appreciate significant variations in the densities of the hot corona and in the atmospheric escape.

[42] Although Figure 4a provides the long-term periodic variations due to seasons and solar activity, a spacecraft would also have to take into account spatial variations. The most important being the decrease due to altitude (1-D symmetrical), then the day-to-night (2-D axisymmetric), and finally the local features (full 3-D), as demonstrated in the study of *Valeille et al.* [2009c]. Recent papers [*Kaneda et al.*, 2007, 2009] indicate a possible mechanism that can cause a short-term (about 2000 s period) enhancement of the hot oxygen escape rate in response to a sudden increase in the solar wind dynamic pressure. The escape rate was found to increase by a factor of about two; and it should be noticed that these results, if somewhat smaller than the total influence of the seasonal variation and the solar cycle, are of the same order.

4. Evolution Over Martian History

[43] The question of how much water exists on Mars today and in the past is still hotly debated, especially when it implies the possibility of life. The oxygen escape rate is known to be a good approximation of water loss from the planet [*Hodges*, 2002]. CO_2 is the obvious parent of escaping O, and reoxidation of the CO produced implies destruction of water.

[44] Planetary escape mechanisms depend on densities of the main constituents (O, CO_2, O_2^+ on Mars), temperatures and winds in the upper thermosphere. Solar radiation affects all those parameters, thus the evolution of planetary atmospheres must be understood within the context of the evolving solar energy and solar wind conditions. A model of the evolving EUV luminosity [*Ribas et al.*, 2005], taken from a study of the Sun in Time program and based on observations of solar-type stars, is used as a guide in adjusting conditions to represent the past.

[45] In this study, not only are enhancements in the solar EUV fluxes considered for the early Sun, but also the decrease in the IR, affecting both the thermosphere/ionosphere and the exosphere. IR fluxes are scaled by a factor 0.79, consistent with the "weak" young Sun [*Guinan and Ribas*, 2002].

[46] Therefore, and for the sake of clarity, three epochs of the solar system are defined. Those correspond to: present (denoted by epoch 1), $\sim$2.7 Gyr ago (epoch 2), and $\sim$3.6 Gyr ago (epoch 3). This notation is closely related to the one used by past studies tied to the EUV flux enhancement in the past and often denoted 1 EUV, 3 EUV, 6 EUV. Epoch 1 corresponds to present solar conditions ($\times 1$ EUV, $\times 1$ IR), epoch 2 corresponds to 3 times the present solar EUV flux and 0.79 times the present solar IR flux ($\times 3$ EUV, $\times 0.79$ IR), and epoch 3 corresponds to 6 times the present solar EUV flux and 0.79 times the present solar IR flux ($\times 6$ EUV, $\times 0.79$ IR).

[47] In the remainder of this paper, all calculations are run for the EL case for the three different epochs. As suggested by the study of *Chassefière et al.* [2007] and demonstrated in the work of *Valeille et al.* [2009b], 11-year periodic variations in the hot corona are comparable to the evolution over the last $\sim$3.6 Gyr. Therefore, calculations presented here only provide a lower limit of the evolution of the Martian upper atmosphere over history. More detail in the assumptions and results for the equinox solar high case for the three different epochs, can be found in the study of *Valeille et al.* [2009b].

4.1. Thermosphere/Ionosphere

[48] A general discussion about the thermosphere structure of these epochs was conducted in a previous study [*Valeille et al.*, 2009b] in order to estimate the water loss over the Martian history. In the current study, the results are presented at the respective exobase level for each epoch in order to quantify the influence of the solar radiation onto the early Mars upper atmosphere and compare them with variations of smaller time scales (see section 3.1). Similar to the influence of the solar cycle, the influence of the epochs affects the magnitude of most of the thermospheric parameters, while their general spatial distribution is mostly unchanged.

4.1.1. Temperatures, Heating, and Winds

[49] Figures 5b, 5d, and 5f show the neutral temperatures and winds at the respective exobase level for epoch 1, 2, and 3, respectively. The general temperature structure is not significantly different in the past, with minima situated south at low and middle latitudes on the nightside. Maxima are located on the dayside in the polar regions and vicinity of the evening terminator, with the exception for the extreme case of epoch 3 where maxima are closer to the subsolar point (Figure 5f). The average neutral temperature, T_∞, (170, 260, and 360 K), the amplitude between extrema

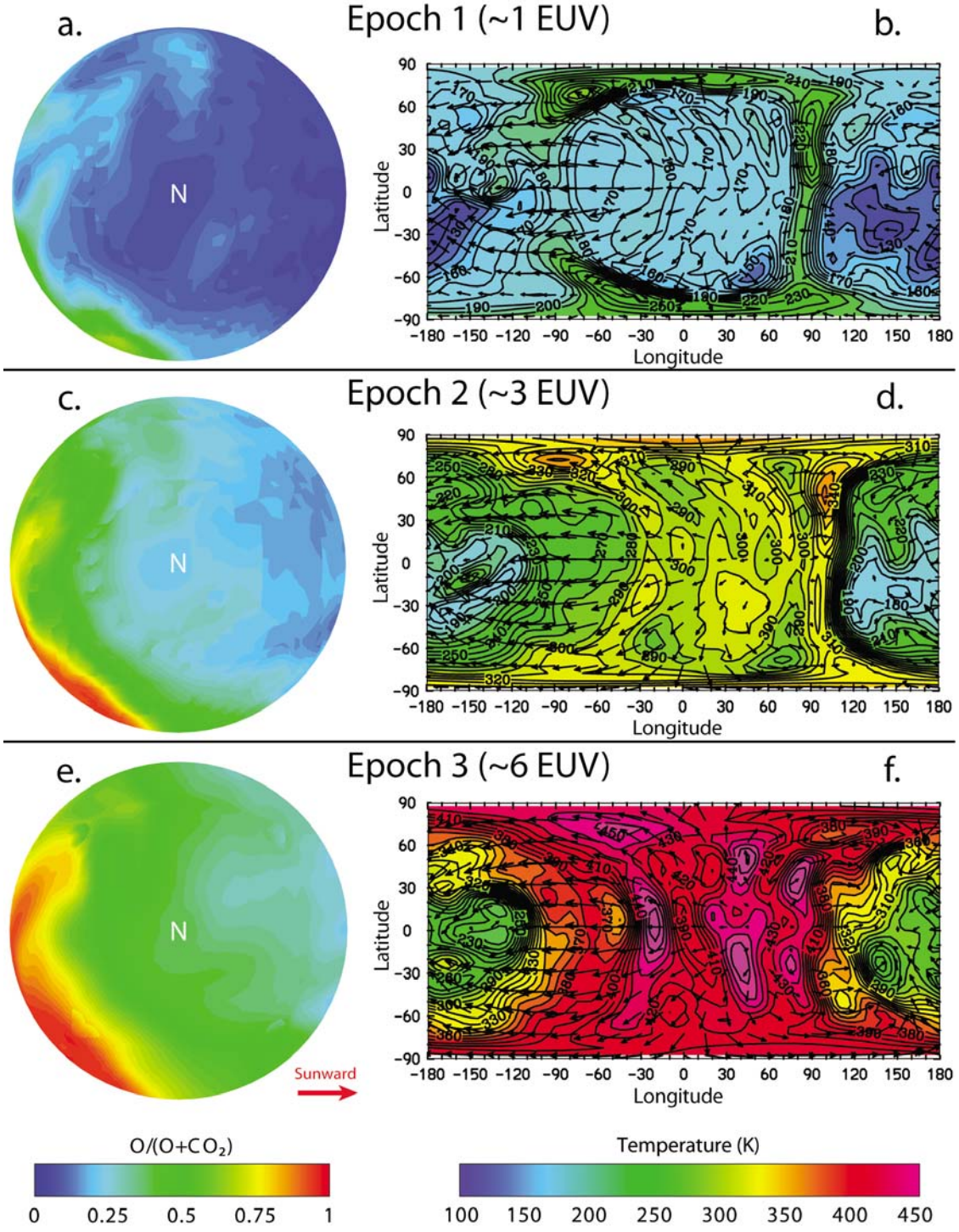

Figure 5. (a, c, and e) Oxygen mixing ratio in the winter hemisphere and (b, d, and f) neutral temperature in the vicinity of Mars exobase at epoch 1, 2, and 3. The results are shown for the EL conditions at the respective average exobase level, i.e., at an altitude of 170, 190, and 220 km for epoch 1 (Figures 5a and 5b), epoch 2 (Figures 5c and 5d), and epoch 3 (Figures 5e and 5f), respectively. Horizontal wind velocities are represented in the frame associated with Mars by arrows with maxima at ~490 (Figure 5b), ~530 (Figure 5d), and ~610 m s^{-1} (Figure 5f). The same color scale is used for each image and is consistent with that for Figure 1. The north and south pole positions are indicated by N and S, respectively. The red arrow points toward the Sun.

(+180, +200, and +260 K) and the day-to-night dynamics (490, 530, and 610 m s^{-1}) increase significantly with higher EUV fluxes consistent with ancient Mars conditions (for epoch 1, 2, and 3, respectively).

[50] It is important to notice that subsolar temperatures are still under the basic control of local EUV-UV heating and molecular thermal conduction, even as solar fluxes are enhanced for ancient Mars conditions. However, the impact of global winds (i.e., upwelling and associated adiabatic cooling) becomes progressively more important as solar fluxes are enhanced (epoch 2 and 3). This is consistent with the growing magnitude of global winds for these ancient Mars simulations.

[51] In addition, CO_2 15-μm cooling becomes progressively more important into the past. This situation results from the growing atomic O abundance as CO_2 net dissociation is enhanced for larger solar EUV-UV fluxes for ancient Mars conditions. In fact, CO_2 15-μm cooling shows a significant role for balancing dayside EUV-UV heating at epoch 3, a condition similar to present-day Venus conditions [*Bougher et al.*, 1999]. This important result suggests that the ancient Mars thermosphere (of about 3.6 Gyr ago) was very similar to the present Venus not only in terms of bulk composition, but also in terms of heat balances. This similarity between present Venus and ancient Mars could be explained by the fact that, the solar flux at Venus ($\sim$0.7 AU) is about 4.5 times that of Mars ($\sim$1.5 AU) for present conditions (and therefore somewhat close to the ancient Mars conditions at epoch 3) [*Valeille et al.*, 2009b].

4.1.2. O and CO_2 Density Distribution

[52] The O to CO_2 ratio is a particularly important parameter of the Martian upper atmosphere, as both species are present at comparable abundances in the vicinity of the exobase. The ratio affects the exobase height, the plasma heating, as well as the escape loss due to incident pickup ions [*Leblanc and Johnson*, 2002]. Figures 5a, 5c, and 5e present the O mixing ratio at respective exobase heights for epoch 1, 2, and 3, respectively. The O mixing ratio exhibits the same structure in the past and at present, with a clear day-to-night difference. Minima are on the dayside at low northern latitudes, maxima at low southwest latitudes. The average value of the O mixing ratio at the exobase increases due to a higher exobase altitude in the past. Also, stronger winds result in higher O abundances on the nightside. At a given altitude, an enhancement in density of a factor about $\times$13 is estimated between epoch 1 and 3. This increase in the background densities at a fixed altitude is due to higher thermospheric temperatures in the past, which affect the scale heights of the constituents proportionally, resulting in a general expansion of the atmosphere.

[53] The ion production is expected to be higher at places where CO_2 is dominant locally. So would be the plasma heating, whereas the sputtering yield and the escape loss due to incident pickup ions should decrease due to a lower atom-to-molecule ratio [*Leblanc and Johnson*, 2002].

4.1.3. O_2^+ Distribution and Ionospheric Peak

[54] As mentioned above in the study of thermospheric/ionospheric variations with solar cycle, the ion peak height is controlled by the underlying atmosphere, and therefore is not responsive to an increase in the EUV flux. The same altitude of $\sim$120 km is computed for all three epochs, suggesting that the ion peak level may have stayed constant in the past. However, the magnitude of the ion density increases significantly with EUV, with the simulated electron density at the peak being 2.0, 3.4, and 4.7 $\times$ 10^5 cm^{-3} at the subsolar point for epochs 1, 2, and 3, respectively. Those values can be compared to the corresponding values of O_2^+ abundance given in the work of *Valeille et al.* [2009b]. The results presented here fall between theory [*Cravens et al.*, 1981; *Schunk and Nagy*, 2009] and observations [*Breus et al.*, 2004]. The magnitude of the ion peak decreases with SZA, but the decrease is relatively more important at present than in the past by about a factor $\times$0.4 for epoch 1 and $\times$0.5 for epochs 2 and 3, between 0° and 75° SZA.

4.1.4. Exobase Altitude

[55] The average exobase level is found to be significantly higher for past solar conditions (170, 190, and 220 km altitude for epoch 1, 2, and 3, respectively). Those values are significantly less than the average 1-D estimates of previous studies [*Zhang et al.*, 1993b; *Lammer et al.*, 2003]. This is due mostly to the inclusion of the cooling effect of the day-to-night dynamics in the current MTGCM study. In this regard, horizontal and vertical winds can be seen as a thermostat regulating the effect of the increase of the past solar EUV fluxes in the Martian thermosphere [*Valeille et al.*, 2009b].

4.2. Exosphere

[56] Figures 6a, 6c, and 6e show that the spatial extent of the hot corona may have been very inflated for past epochs. At a given altitude, a uniform global enhancement of density by factors of about $\times$5–6 and $\times$14 is estimated between epochs 1 and 2, and epochs 1 and 3, respectively. The total escape rate (in Figures 6b, 6d, and 6f) increases from 6.0 $\times$ 10^{25} s^{-1} for epoch 1, to 2.2 $\times$ 10^{26} s^{-1} for epoch 2, and to 5.7 $\times$ 10^{26} s^{-1} for epoch 3 (Table 3).

[57] The model provides maps of the three main ionization processes, i.e., photoionization (PI), charge exchange (CE), and electron impact (EI), as explained in detail in the study of [*Valeille et al.*, 2009b]. The respective PI, CE, and EI frequencies are derived from past studies [*Stebbings et al.*, 1964; *Cravens et al.*, 1987; *Bailey and Sellek*, 1990]. Estimated positions of the ionopause and bow shock [*Zhang et al.*, 1993a; *Leblanc and Johnson*, 2001; *Trotignon et al.*, 2006] are used.

[58] The simulated total ionization rate in the Martian ionosphere after summation of the three main ionization contributions is presented in Table 3. For present conditions, integration gives a total O^+ ion production of 2.2 $\times$ 10^{24} s^{-1}, and 1.0 $\times$ 10^{25} s^{-1} for the EL case and the EH case, respectively, in good agreement with the recent study of *Chaufray et al.* [2007] (1.9 $\times$ 10^{24} s^{-1} and 9.4 $\times$ 10^{24} s^{-1}, respectively). Under the generous assumption that all ions produced above 300 km escape [*Zhang et al.*, 1993b], the computed O^+ ion loss would then be in excellent agreement with the respective values for EL and EH for present conditions of $\sim$2.4 $\times$ 10^{24} s^{-1} and $\sim$1.0 $\times$ 10^{25} s^{-1} based on data obtained with new energy settings for ASPERA-3 ion mass analyzer (IMA) on MEX reported in the recent study of *Lundin et al.* [2008].

[59] The ion production appears to increase more dramatically (about a factor $\times$160) with higher EUV radiation in the past, from 2.2 $\times$ 10^{24} s^{-1} for epoch 1 to 3.5 $\times$ 10^{26} s^{-1}

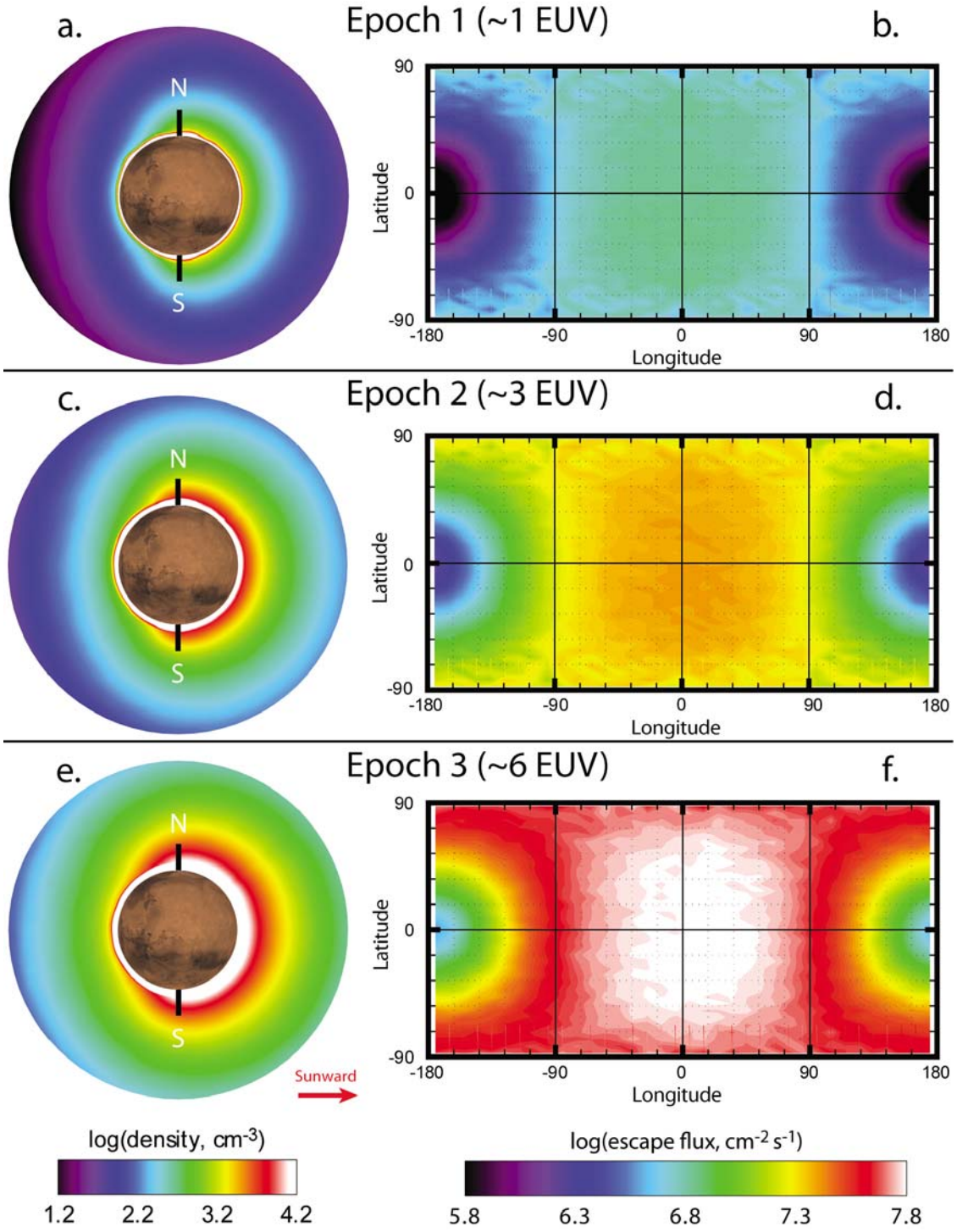

Figure 6. (a, c, and e) Density profiles (b, d, and f) and escape fluxes at 3 Martian radii of oxygen atoms at epoch 1, 2, and 3. The results are shown for the EL conditions. The same color scale is used for each image and is consistent with that for Figures 2 and 3. The north and south pole positions are indicated by N and S, respectively. The red arrow points toward the Sun.

Table 3. Neutral Oxygen Escape and O^+ Ion Production Rates for Epochs 1, 2, and 3[a]

	Epoch 1 (~1 EUV)		Epoch 2 (~3 EUV)		Epoch 3 (~6 EUV)	
	Solar Low	Solar High	Solar Low	Solar High	Solar Low	Solar High
O escape by DR	6.0×10^{25}	1.9×10^{26}	2.2×10^{26}		5.7×10^{26}	
O^+ production	2.2×10^{24}	1.0×10^{25}	3.8×10^{25}		3.5×10^{26}	

[a]Ion production rates are measured in s^{-1}.

Table 4. Variations in Magnitude and Spatial Distribution for Thermospheric/Ionospheric and Exospheric Parameters due to Seasons, Solar Cycle, and History[a]

	Season (∼2 yr)	Solar Cycle (∼11 yr)	History (∼3.5 Gyr)
Variations in the Thermosphere			
Temperatures[b] (ΔT)	small (20 K)	moderate (100 K)	important (190 K)
Spatial distribution[c]	important	none	small
Exobase height (Δz)	moderate (15 km)	moderate (15 km)	important (50 km)
Spatial distribution[c]	important	none	none
O density[d] (n/n0)	moderate (×1.7–1.8)	moderate (×1.8–2.0)	important (×13)
Spatial distribution[c]	important	none	none
Ion peak height (Δz)	moderate (12 km)	none	none
Spatial distribution[c]	important	none	none
Electron density[e] (n/n0)	small (×1.2)	moderate (×1.5–1.6)	important (×2.4)
Spatial distribution[c]	important	none	none
Variations in the Exosphere			
O density (n/n_0)	small (×∼1.2)	moderate (×3)	important (×14)
Spatial distribution[c]	small	none	small
O escape (φ/φ_0)	small (×1.6)	moderate (×3–4)	important (×6–9)
Spatial distribution[c]	small	none	none
O^+ production (χ/χ_0)		moderate (×4–5)	important (×∼160)
Spatial distribution[c]	small	none	none

[a]Seasons, comparing aphelion to perihelion; solar cycle, comparing solar low to solar high; history, comparing epoch 1 to 3.
[b]Results for neutral temperature could be extended to electron and ion temperature if they are assumed tied *Fox et al.* [1995, also private communication, 2008].
[c]Spatial distribution refers to the angular distribution around the planet in the frame associated with the Sun.
[d]CO_2 density and O mixing ratio can be inferred from the results for O density.
[e]At the ion peak rather than at the exobase altitude.

for epoch 3. However, even though the O_2^+ DR contribution to the total oxygen escape might have been smaller in the past compared to the present secondary processes, integration over time shows that it is still the most important process in loss of water over the Martian history [*Valeille et al.*, 2009b]. The integration of the calculated loss rates leads to a total loss of about 10 m of water to space over the last ∼3.5 Gyr, in agreement with previous studies of *Lammer et al.* [2003] and *Kulikov et al.* [2007], suggesting that the bulk of water escape on Mars had happened during the first Gyr of the planet. However, other competing processes, such as cool ion outflow [*Terada et al.*, 2009], thermal escape [*Tian et al.*, 2009], impact erosion [e.g., *Pham et al.*, 2009], become important at that time and should then also be considered. A more detailed discussion about the water loss of the Martian atmosphere in the last ∼3.5 Gyr and before can be found in the study of *Valeille et al.* [2009b].

5. Conclusion

[60] In this study, the combination of the 3-D DSMC kinetic model and the 3-D MTGCM is used to provide for the first time a self-consistent 3-D description of the variations in the Martian upper atmosphere over long-term and evolutionary time scales. A brief summary of the variations of the main parameters in the thermosphere/ionosphere and in the exosphere is presented in Table 4. The most important conclusion of this work is that spatial, seasonal, solar cycle and evolutionary driven variations are all estimated to be of the same order. For illustration, the atmospheric loss is enhanced by a factor about three locally between day and night at 10 Mars radii, by a factor about two between limiting seasonal cases (AL and PL), by a factor about three between the solar cycle equinox cases (EL and EH) and by a factor about nine between present and ∼3.5 Gyr ancient thermospheres.

[61] This underlines the importance of taking into account both solar cycle and seasonal effects for a rigorous description of the Martian hot corona and the atmospheric loss for modern conditions. Studying the combined effect of both long-term variations would be useful for future mission planning. Also, in order to characterize the global loss of water, studies of the ancient upper atmosphere should consider both solar low and high conditions (or at least consider solar moderate as a solar cycle average in the past) when estimating any EUV-dependent process in the early Mars.

[62] The results for modern conditions show that the escape rate varies from 4.6×10^{25} to 2.6×10^{26} s^{-1} between the two extreme cases of net solar forcing (i.e., between the AL and PH cases). While the exobase height varies with seasons and solar activity (from 165 to 195 km altitude for the AL and PH case, respectively), the ion peak height varies exclusively with seasons (122 ± 6 km altitude).

[63] The study of the evolution of the heat balance suggests that the ancient Mars thermosphere (of about 3.5 Gyr ago) was relatively similar to the present Venus thermosphere. The escape rate is estimated to be 5.7×10^{26} s^{-1} at that epoch, corresponding to a total loss of about 10 m of water to space over the last ∼3.5 Gyr.

[64] **Acknowledgments.** Support for this work comes from the NASA Mars Fundamental Research grant NNG05GL80G and the Mars Data Analysis Program grant NNX07AO84G. Computations were performed on the massively parallel Columbia computer at the High-End Computing (HEC) Program's NASA Advanced Supercomputing (NAS) Facility. The authors are grateful to the collective of the Solar Influences Data analysis Center (SIDC) at the Royal Observatory of Belgium (ROB) for data sets.

References

Bertaux, J.-L., et al. (2005), Nightglow in the upper atmosphere of Mars and implications for atmospheric transport, *Science*, *307*, 566–569, doi:10.1126/science.1106957.

Bougher, S. W., S. Engel, R. G. Roble, and B. Foster (1999), Comparative terrestrial planet thermospheres: 2. Solar cycle variation of global struc-

ture and winds at equinox, *J. Geophys. Res.*, *104*, 16,591–16,611, doi:10.1029/1998JE001019.

Bougher, S. W., S. Engel, R. G. Roble, and B. Foster (2000), Comparative terrestrial planet thermospheres: 3. Solar cycle variation of global structure and winds at solstices, *J. Geophys. Res.*, *105*, 17,669–17,692, doi:10.1029/1999JE001232.

Bougher, S. W., S. Engel, D. P. Hinson, and J. R. Murphy (2004), MGS Radio Science electron density profiles: Interannual variability and implications for the neutral atmosphere, *J. Geophys. Res.*, *109*, E03010, doi:10.1029/2003JE002154.

Bougher, S. W., J. M. Bell, J. R. Murphy, P. G. Withers, and M. López-Valverde (2006), Polar warming in the Mars lower thermosphere: Seasonal variations owing to changing insolation and dust distributions, *Geophys. Res. Lett.*, *33*, L02203, doi:10.1029/2005GL024059.

Bougher, S. W., P.-L. Blelly, M. Combi, J. L. Fox, I. Mueller-Wodarg, A. Ridley, and R. G. Roble (2008), Neutral upper atmosphere and ionosphere modeling, *Space Sci. Rev.*, *139*, 107–141, doi:10.1007/s11214-008-9401-9.

Bougher, S. W., T. M. McDunn, K. A. Zoldak, and J. M. Forbes (2009), Solar cycle variability of Mars dayside exospheric temperatures: Model evaluation of underlying thermal balances, *Geophys. Res. Lett.*, *36*, L05201, doi:10.1029/2008GL036376.

Breus, T. K., A. M. Krymskii, D. H. Crider, N. F. Ness, D. Hinson, and K. K. Barashyan (2004), Effect of the solar radiation in the topside atmosphere/ionosphere of Mars: Mars Global Surveyor observations, *J. Geophys. Res.*, *109*, A09310, doi:10.1029/2004JA010431.

Chassefière, E., F. Leblanc, and B. Langlais (2007), The combined effects of escape and magnetic field histories at Mars, *Planet. Space Sci.*, *55*, 343–357, doi:10.1016/j.pss.2006.02.003.

Chaufray, J. Y., R. Modolo, F. Leblanc, G. Chanteur, R. E. Johnson, and J. G. Luhmann (2007), Mars solar wind interaction: Formation of the Martian corona and atmospheric loss to space, *J. Geophys. Res.*, *112*, E09009, doi:10.1029/2007JE002915.

Cravens, T. E., A. J. Kliore, J. U. Kozyra, and A. F. Nagy (1981), The ionospheric peak on the Venus dayside, *J. Geophys. Res.*, *86*, 11,323–11,329, doi:10.1029/JA086iA13p11323.

Forbes, J. M., F. G. Lemoine, S. L. Bruinsma, M. D. Smith, and X. Zhang (2008), Solar flux variability of Mars' exosphere densities and temperatures, *Geophys. Res. Lett.*, *35*, L01201, doi:10.1029/2007GL031904.

Guinan, E. F., and I. Ribas (2002), Our changing sun: The role of solar nuclear evolution and magnetic activity on Earth's atmosphere and climate, in *The Evolving Sun and its Influence on Planetary Environments*, *Astron. Soc. Pac. Conf. Ser.*, *269*, 85–106.

Haberle, R. M., M. M. Joshi, J. R. Murphy, J. R. Barnes, J. T. Schofield, G. Wilson, M. López-Valverde, J. L. Hollingsworth, A. F. C. Bridger, and J. Schaeffer (1999), General circulation model simulations of the Mars Pathfinder atmospheric structure investigation/meteorology data, *J. Geophys. Res.*, *104*, 8957–8974, doi:10.1029/1998JE900040.

Hanson, W. B., S. Santanini, and D. R. Zuccaro (1977), The Martian ionosphere as observed by Viking retarding potential analyszers, *J. Geophys. Res.*, *82*, 4351–4363, doi:10.1029/JS082i028p04351.

Hodges, R. R. (2000), Distributions of hot oxygen for Venus and Mars, *J. Geophys. Res.*, *105*, 6971–6981, doi:10.1029/1999JE001138.

Hodges, R. R. (2002), The rate of loss of water from Mars, *Geophys. Res. Lett.*, *29*(3), 1038, doi:10.1029/2001GL013853.

Ip, W. H. (1990), The fast atomic oxygen corona extent of Mars, *Geophys. Res. Lett.*, *17*, 2289–2292, doi:10.1029/GL017i013p02289.

Kaneda, K., N. Terada, and S. Machida (2007), Time variation of nonthermal escape of oxygen from Mars after solar wind dynamic pressure enhancement, *Geophys. Res. Lett.*, *34*, L20201, doi:10.1029/2007GL030576.

Kaneda, K., N. Terada, and S. Machida (2009), Solar-wind control of the hot-oxygen corona around Mars, *J. Geophys. Res.*, *114*, E02007, doi:10.1029/2008JE003234.

Kella, D., P. J. Johnson, H. B. Pederson, L. Vejby-Christensen, and L. H. Andersen (1997), The source of green light emission determined from a heavy-ion storage ring experiment, *Science*, *276*, 1530–1533, doi:10.1126/science.276.5318.1530.

Kim, Y. H., S. Son, Y. Yi, and J. Kim (2001), A non-spherical model for the hot oxygen corona of Mars, *J. Korean Astron. Soc.*, *34*, 25–29.

Kulikov, Y. N., H. Lammer, H. I. M. Lichtenegger, T. Penz, D. Breuer, T. Spohn, R. Lundin, and H. K. Biernat (2007), Comparative study of the influence of the active young Sun on the early atmospheres of Earth, Venus, and Mars, *Space Sci. Rev.*, *129*, 207–243, doi:10.1007/s11214-007-9192-4.

Lammer, H., H. I. M. Lichtenegger, C. Kolb, I. Ribas, E. F. Guinan, R. Abart, and S. J. Bauer (2003), Loss of water from Mars: Implications for the oxidation of soil, *Icarus*, *165*, 9–25, doi:10.1016/S0019-1035(03)00170-2.

Leblanc, F., and R. E. Johnson (2001), Sputtering of the Martian atmosphere by solar wind pick-up ions, *Planet. Space Sci.*, *49*, 645–656, doi:10.1016/S0032-0633(01)00003-4.

Leblanc, F., and R. E. Johnson (2002), Role of molecular species in pickup ion sputtering of the Martian atmosphere, *J. Geophys. Res.*, *107*(E2), 5010, doi:10.1029/2000JE001473.

López-Valverde, M. A., D. P. Edwards, M. López-Puertas, and C. Roldán (1998), Nonlocal thermodynamic equilibrium in general circulation models of the Martian atmosphere: 1. Effects of the local thermodynamic equilibrium approximation on thermal cooling and solar heating, *J. Geophys. Res.*, *103*, 16,799–16,812, doi:10.1029/98JE01601.

Lundin, R., S. Barabash, M. Holmström, H. Nilsson, M. Yamauchi, M. Fraenz, and E. M. Dubinin (2008), A comet-like escape of ionospheric plasma from Mars, *Geophys. Res. Lett.*, *35*, L18203, doi:10.1029/2008GL034811.

Mehr, F. J., and M. A. Biondi (1969), Electron temperature dependence of recombination of O_2^+ and N_2^+ ions with electrons, *Phys. Rev.*, *181*, 264–271, doi:10.1103/PhysRev.181.264.

Morgan, D. D., D. A. Gurnett, D. L. Kirchner, J. L. Fox, E. Nielsen, and J. J. Plaut (2008), Variation of the Martian ionospheric electron density from Mars Express radar soundings, *J. Geophys. Res.*, *113*, A09303, doi:10.1029/2008JA013313.

Nier, A. O., and M. B. McElroy (1977), Composition and structure of Mars' upper atmosphere: Results from the neutral mass spectrometers on Viking 1 and 2, *J. Geophys. Res.*, *82*, 4341–4349, doi:10.1029/JS082i028p04341.

Pham, L. B. S., Ö. Karatekin, and V. Dehant (2009), Effects of meteorite impacts on the atmospheric evolution of Mars, *Astrobiology*, *9*, 45–54, doi:10.1089/ast.2008.0242.

Podladchikova, T., B. Lefebvre, and R. A. M. Van der Linden (2007), Integral activity of the declining phase of sunspot cycles as precursor of the next cycle, *J. Atmos. Sol. Terr. Phys.*, *70*, 277–284, doi:10.1016/j.jastp.2007.08.068.

Ribas, I., E. F. Guinan, M. Gudel, and M. Audard (2005), Evolution of the solar activity over time and effects on planetary atmospheres: I. High-energy irradiances (1–1700 Å), *Astrophys. J.*, *622*, 680–694, doi:10.1086/427977.

Schunk, R. W., and A. F. Nagy (2009), *Ionospheres*, Cambridge Univ. Press, New York.

Stebbings, R. F., A. C. H. Smith, and H. Erhardt (1964), Charge transfer between oxygen atoms and O+ and H+ ions, *J. Geophys. Res.*, *69*, 2349–2355, doi:10.1029/JZ069i011p02349.

Stewart, A. I. F. (1987), Revised time dependent model of the Martian atmosphere for use in orbit lifetime and sustenance studies, *LASP-JPL Internal Rep. PO# NQ-802429*, Jet Propul. Lab., Pasadena, Calif.

Tenishev, V., M. R. Combi, and B. Davidsson (2008), A global kinetic model for cometary comae: The evolution of the coma of the Rosetta target comet Churyumov-Gerasimenko throughout the mission, *Astrophys. J.*, *685*, 659–677, doi:10.1086/590376.

Terada, N., Y. N. Kulikov, H. Lammer, H. I. M. Lichtenegger, T. Tanaka, H. Shinagawa, and Z. Zhang (2009), Atmosphere and water loss from early Mars under extreme solar wind and extreme ultraviolet conditions, *Astrobiology*, *9*, 55–70, doi:10.1089/ast.2008.0250.

Tian, F., J. F. Kasting, and S. C. Solomon (2009), Thermal escape of carbon from the early Martian atmosphere, *Geophys. Res. Lett.*, *36*, L02205, doi:10.1029/2008GL036513.

Trotignon, J. G., C. Mazelle, C. Bertucci, and M. H. Acuna (2006), Martian shock and magnetic pile-up boundary positions and shapes determined from Phobos 2 and Mars Global Surveyor data sets, *Planet. Space Sci.*, *54*, 357–369, doi:10.1016/j.pss.2006.01.003.

Valeille, A., M. R. Combi, V. Tenishev, S. W. Bougher, and A. F. Nagy (2009a), A study of suprathermal oxygen atoms in Mars upper thermosphere and exosphere over the range of limiting conditions, *Icarus*, doi:10.1016/j.icarus.2008.08.018, in press.

Valeille, A., S. W. Bougher, V. Tenishev, M. R. Combi, and A. F. Nagy (2009b), Water loss and evolution of the upper atmosphere and exosphere over Martian History, *Icarus*, doi:10.1016/j.icarus.2009.04.036, in press.

Valeille, A., S. W. Bougher, V. Tenishev, M. R. Combi, and A. F. Nagy (2009c), Three-dimensional study of Mars upper thermosphere/ionosphere and hot corona: 1. General description and results at equinox for solar minimum conditions, *J. Geophys. Res.*, *114*, E11005, doi:10.1029/2009JE003388.

Withers, P., and M. Mendillo (2005), Response of peak electron densities in the Martian ionosphere to day-to-day changes in solar flux due to solar rotation, *Planet. Space Sci.*, *53*, 1401–1418, doi:10.1016/j.pss.2005.07.010.

Zhang, M. H. G., J. G. Luhmann, and A. J. Kliore (1990), An observational study of the nightside ionospheres of Mars and Venus with radio occultation methods, *J. Geophys. Res.*, *95*, 17,095–17,102, doi:10.1029/JA095iA10p17095.

Zhang, M. H. G., J. G. Luhmann, and A. F. Nagy (1993a), Oxygen ionization rates at Mars and Venus: Relative contributions of impact ionization and charge exchange, *J. Geophys. Res.*, *98*, 3311–3318, doi:10.1029/92JE02229.

Zhang, M. H. G., J. G. Luhmann, S. W. Bougher, and A. F. Nagy (1993b), The ancient oxygen exosphere of Mars: Implications for atmosphere evolution, *J. Geophys. Res.*, *98*, 10,915–10,923, doi:10.1029/93JE00231.

S. W. Bougher, M. R. Combi, A. F. Nagy, V. Tenishev, and A. Valeille, Department of Atmospheric, Oceanic and Space Sciences, Space Research Building, University of Michigan, 2455 Hayward Street, Ann Arbor, MI 48109-2143, USA.